Title
Effect of Varied Air Flow on Flame Structure of Laminar Inverse Diffusion Flames

Authors
Mikofski, Mark A
Williams, Timothy C
Shaddix, Christopher R
et al.

Publication Date
2004-03-01

Peer reviewed

Effect of Varied Air Flow on Flame Structure of Laminar Inverse Diffusion Flames

Western States Section/Combustion Institute
2004 Spring Meeting

Paper Number: 04S-7

Mark A. Mikofski*
University of California Berkeley

Timothy C. Williams, Christopher R. Shaddix, and Linda G. Blevins
Sandia National Laboratories, Livermore, CA

*Corresponding author: mikofski@me.berkeley.edu

Effect of Varied Air Flow on Flame Structure of Laminar Inverse Diffusion Flames

Mark A. Mikofski
University of California Berkeley

Timothy C. Williams, Christopher R. Shaddix, and Linda G. Blevins
Sandia National Laboratories, Livermore, CA

Abstract
The structure of laminar inverse diffusion flames (IDFs) of methane and ethylene was studied using a cylindrical co-flowing burner. Several flames of the same fuel flow-rate yet various air flow-rates were examined. Heights of visible flames were obtained using measurements of hydroxyl (OH) laser-induced fluorescence (LIF) and visible images. Polycyclic aromatic hydrocarbon (PAH) LIF and soot laser-induced incandescence (LII) were also measured. In visible images, radiating soot masks the blue region typically associated with the flame height in normal diffusion flames (NDFs). Increased air flow-rates resulted in longer flames. PAH LIF and soot LII indicated that PAH and soot are present on the fuel side of the flame and that soot is located closer to the reaction zone than PAH. Ethylene flames produced significantly higher PAH LIF and soot LII signals than methane flames, which is consistent with the sooting propensity of ethylene.

Introduction

Inverse diffusion flames are similar to normal diffusion flames, except that the relative positions of the fuel and oxidizer are reversed. Inverse diffusion flames are similar to underventilated combustion found in accidental fires [1,2,6], and many staged air burners use an IDF configuration. In addition, IDFs have significant emissions of soot, PAH, CO, and other carbon containing species, which form on the outside of the flame in the fuel region and escape the flame unoxidized. The study of IDFs may reveal information about the formation of these emissions because they form outside the reaction zone and are easier to examine without significantly disturbing the flame.

The aim of the research presented in this paper is to examine the basic structure of IDFs by using OH and PAH LIF and soot LII. Radiating soot obscures the blue region of the flame associated with the reaction zone, so visible images may not reveal information about the flame structure. The position of the reaction zone can be found by examining the position of OH LIF. The relative positions of soot and PAH with respect to the reaction zone can be found using soot LII and OH and PAH LIF. The objectives of this paper are (1) to examine the relationship between flame heights obtained from visible images, OH LIF, and a simple scaling analysis, and (2) to gain insight into the IDF soot formation process using planar imaging of OH LIF, PAH LIF, and soot LII.

Experimental Methods

The cylindrical co-annular jet burner used in this research has a 1 cm diameter central air tube. Fuel flows in the annulus between a 3 cm diameter tube and the central air tube. Table 1 lists the air and fuel flow-rates and other operating conditions for the methane

and ethylene flames tested. The volumetric flow-rates of fuel and air are represented by Q_{fuel} and Q_{air}, respectively. The average velocities of the fuel and air at the burner exit are given by V_{fuel} and V_{air}, respectively. The Reynolds number for the fuel, $Re_{fuel,Dc}$, is based on the cold-flow conditions of the fuel at the burner exit and the hydraulic diameter, $D_c = 2$ cm. The Reynolds number for the air, $Re_{air,Dair}$, is based on the cold-flow conditions of the air at the burner exit and D_{air}. The overall equivalence ratio, defined as the fuel-to-air ratio divided by the stoichiometric fuel-to-air ratio, is given by $\Phi_{overall}$. The estimated heat release rate, HRR_{air}, is based on the heating value of the fuel assuming all of the air reacts completely.

For visible images, the burner was placed inside a sealed 27 L chamber filled with nitrogen to 1 atm to prevent secondary flames from forming between the fuel and ambient air. The chamber was used to prevent cross flows from affecting the stability of the flames. Tests in the chamber were conducted for 2 seconds and the chamber pressure typically rose from 14.7 psia to 14.9 psia. A glass window provided optical access with 96% transmission from 0.3 to 2.0 μm, and a charge-coupled device (CCD) camera with a resolution of 640 x 480 pixels was used to record flame images at a rate of 30 frames per second. The sealed chamber and the 2 second protocol were used to facilitate future comparisons to microgravity drop tower experiments. Previous work revealed that IDFs on the present burner achieve steady-state conditions within 0.5 seconds.

To prevent secondary flames from forming during LIF and LII measurements, nitrogen flowed at a rate of 30 slpm through a second annulus formed between a 6.4 cm diameter tube and the 3 cm diameter tube. The average cold-flow velocity of the nitrogen co-flow was 20 cm/s. Over a distance of 2 cm, typical of the flame length, momentum from the co-flow would diffuse approximately 1 mm into the neighboring fuel steam. Since the fuel stream is 1 cm thick, the effect of the nitrogen co-flow was considered negligible. The burner was not enclosed in the chamber used for visible images. It was instead surrounded by a metal shield 30 cm high, placed approximately 20 cm from each side of the burner, forming a rectangle around the burner. An opening 5 cm high was made to admit the laser light. A hood serviced by a 45,000 L/min (1,500 cfm) fan above the burner provided ventilation of the post-combustion gases and unburned fuel.

A frequency-doubled, Nd:YAG-pumped dye laser provided pulsed ultraviolet light for the simultaneous planar excitation of OH and PAH fluorescence [10]. The laser light also excited laser-induced incandescence (LII) emission from the soot particles [9]. The laser sheet was 50 mm high, with a thickness of 250 μm through the flame zone. The beam was used to pump the relatively temperature-insensitive $Q_{21}(8)$ line of the (1,0) band of the OH· $A^2\Sigma^+ \leftarrow X^2\Pi_i$ electronic transition at 283.586 nm. The fluorescence and LII signals were collected through a 105 mm focal length, f/4.5 UV Nikkor lens attached to a gated, intensified charge-coupled device (ICCD) camera. A 295 nm long-pass filter eliminated laser reflections as well as scattering from soot particles. For the fluorescence measurements, an additional filter was used to reduce the signal contribution from soot LII, C_2 Swan band emission, and natural flame emission. For imaging, a 450 nm UV-quality short-pass filter was used for methane flames, and a 340 nm band-pass filter was used for ethylene flames, to further attenuate soot LII and better balance the OH and PAH

LIF signals. For analysis of peak OH and PAH LIF, the 340 nm band-pass filter was used with both fuels to compare relative intensities. In both cases, OH and PAH signals could be clearly distinguished by tuning the laser off of the OH absorption line. The ICCD camera does not use a physical shutter, but charges and discharges the ICCD from the outside towards the center over 40 ns. To prevent irising effects from the slow-gating ICCD camera, an intensifier gate width of 200 ns was used for both the fluorescence and LII measurements. All OH and PAH LIF measurements were corrected for beam power profile variation. Laser beam profile variation was measured by observing Raleigh scattering through room temperature air. Shot-to-shot variations in beam profile and laser power were negligible.

For the LII measurements, a 200 ns gate delay was imposed on the ICCD and a 550 nm long-pass filter was used. Even with this long gate delay and long-wavelength filter, some contribution of PAH LIF was evident, but it generally amounted to no more than 10% of the soot LII signals. An image without any laser light was subtracted from each LII image to eliminate flame luminosity. With the use of a UV excitation wavelength and such a long gate delay and gate width, the LII signals should be regarded as semi-quantitative measures of the soot concentration, with some sensitivity to variations in soot primary particle size [9]. Table 2 lists the filter type, camera gate delay, and gain used for the images presented in this paper and for the comparative quantitative analyses presented in this paper.

Flame heights were determined in three ways. First, visible flame heights were determined by using Spotlight imaging software [7]. The average and standard deviation of the visible height were determined from 45 frames in which the flame had reached steady state conditions. The height for each frame was arbitrarily defined as the vertical distance from the base of the flame to the first pixel near the centerline having a grayscale intensity less than 150% of the mean grayscale intensity of each frame. Second, OH LIF flame heights and standard deviations were determined from 100 consecutive LIF-imaging frames. The height was defined as the vertical distance from the base of the flame to the maximum OH LIF intensity near the centerline. Third, a scaling analysis was performed to determine theoretical flame heights. The details of the scaling analysis follow.

Glassman gives a well-known expression for the flame height [5] that is based on equating the advective and diffusive time scales, neglecting buoyancy, and assuming constant density, mass diffusivity and velocity. Since this is an IDF, the air flow-rate rather than the fuel flow-rate is used in the expression taken from Glassman:

$$L_f = \frac{Q_{air}}{\pi D_{fuel-air}}. \tag{1}$$

In the above equation, Q_{air} is the volumetric air flow-rate at the burner exit and $D_{fuel\text{-}air}$ is the mass diffusivity of fuel into air evaluated at the adiabatic flame temperature. According to Eq. (1), the flame height should increase monotonically with air flow-rate.

Because of heat losses, the temperature in the reaction zone will be less than the adiabatic flame temperature. Hence, the actual diffusivity will be smaller than the one derived using the adiabatic flame temperature since mass diffusivity scales with $T^{1.67}$ [5]. In addition, Richardson numbers (Ri) based on the air velocity, buoyant acceleration defined as $\beta\Delta Tg$ [5], and the air tube radius are close to unity for all of the flames tested. Therefore the flames are slightly buoyant flames, and buoyancy should not be neglected.

Considering both heat losses and buoyancy, a better approximation of the height of the reaction zone can be made. The assumption is made that heat losses are such that the flame temperature in the reaction zone is 80% of the absolute adiabatic flame temperature. The acceleration due to buoyancy will scale with $\beta\Delta Tg$, where β is the thermal coefficient of expansion, approximated here as $1/T_{mean}$ (where T_{mean} is the average of the ambient temperature and the assumed flame temperature), and ΔT is the temperature change, approximated as the difference between the ambient temperature and the assumed flame temperature. If the air is accelerated by buoyancy, continuity with the assumption of constant density yields the expression $V_{air}R_{air}^2 = V_fR_f^2$, where V_{air} is the average air velocity at the air tube exit, R_{air} is the radius of the air tube, V_f is the velocity at the flame tip, and R_f is the effective radial diffusion distance [5]. The diffusive time scale becomes

$$t_{diff} = \frac{R_f^2}{D_{actual}} = \frac{V_{air}R_{air}^2}{V_f D_{actual}}. \tag{2}$$

Under buoyant acceleration $V_f = V_{air} + \beta\Delta Tgt_{diff}$. Some manipulation yields

$$V_f = \frac{V_{air}}{2} + \left(\frac{V_{air}^2}{4} + \frac{\beta\Delta Tg V_{air} R_{air}^2}{D_{actual}} \right)^{1/2}$$
$$L_f = \frac{V_{air}^2 R_{air}^2}{D_{actual} V_f} + \frac{\beta\Delta Tg}{2} \left(\frac{V_{air} R_{air}^2}{D_{actual} V_f} \right)^2. \tag{3, 4}$$

Results and Discussion

Figure 1 shows selected visible images of methane flames. Low and high points in the flickering cycle are shown to demonstrate the degree of unsteadiness. Smaller flames appear stable, and flickering is not as evident as it is in the larger flames. As predicted by the scale analysis, flame height scales with air flow-rate. The blue region indicative of the reaction zone is visible for most of the flame, and only a small soot cone sits on the peak. The tip of the blue region is visible in the smallest flames but is obscured slightly in the larger flames. Figure 2 shows selected images of ethylene flames at low and high points in the flickering cycle. The flame heights and degrees of flickering follow trends similar to those in the methane flames. Unlike the methane flames, radiating soot almost entirely covers each ethylene flame, and only a small portion of the blue region is visible near the base of each flame.

Figure 3 shows selected 100-frame-average images of OH and PAH LIF for the methane IDFs with the 450 nm low-pass filter. The 450 nm short-pass filter emphasizes the weak

PAH LIF intensities in the methane flames. All images in Fig. 3 have the same scale to better display the range of intensities and to allow comparison between images of different flow-rates. Figure 4 shows selected 100-frame-average images of OH and PAH LIF intensities for the ethylene IDFs with the 340 nm band-pass filter. The 340 nm band-pass filter attenuates the very strong PAH LIF intensity in ethylene flames to balance the OH LIF. All images in Fig. 4 have the same scale to better display the range of intensities and to allow comparison between images of different flow-rates. The upside-down U shape in each panel of Figs. 3-4 is OH LIF, which indicates the location of the reaction zone of the flame. PAHs are present on the outer (fuel) side of the reaction zone.

Figure 5 displays the heights obtained for all methane and ethylene flames based on the visible images, the OH LIF images, and the scale analysis. The vertical bars on the visible flame heights and OH LIF heights represent one standard deviation in height. The scale analysis yields flame heights quite close to those obtained by OH LIF. As expected, the visible flame heights are greater than the flame heights measured by OH LIF. The increase in flickering as the ethylene flames get longer is evident in the increase in standard deviation.

Figures 6 and 7 show corresponding soot LII images for the selected methane and ethylene flames in Figs. 3 and 4. The images in Fig. 6 are scaled by a common factor. The Fig. 7 images are scaled by a common factor as well, although the factors used for Figs. 6 and 7 are not the same. In the methane flames, the soot LII cannot be distinguished from the PAH LIF, even though these flames have orange soot caps. This is consistent with the fact that methane inverse flames form very little carbonized soot [1]. Figures 1-2 indicate that soot forms higher in the methane flames than in the ethylene flames. Hence, the high-temperature residence time of the methane soot is probably shorter, and the resulting soot concentration and particle sizes may be smaller. This is significant because soot LII intensity scales with soot concentration and particle size [3]. Thus, for methane, although soot may be present, the soot LII intensity may be too low to detect. In the ethylene flames, PAH LIF is vaguely present in the LII images. For ethylene, the soot and PAH are present on the fuel side of the reaction zone, and the soot is closer than the PAH to the flame. This agrees with the fact that soot production occurs close to the flame where temperatures and carbon-containing species concentrations are sufficiently high [4,8].

Figures 8 and 9 show the positions of the maximum OH, PAH, and soot signals (top panels) and the maximum OH, PAH, and soot signals themselves (bottom panels) versus axial position for selected ethylene and methane flames. Three lines representing the left and right sides of the flame and the average of the two sides demonstrate the degree of asymmetry in the flames. The sharp decline in PAH LIF and soot LII intensity near the axial position of 50 mm is an artifact of the experimental method and is caused by the laser light diffracting at the opening in the metal shield surrounding the burner. In ethylene flames, soot LII is present within one centimeter of the base of the flame, indicating that soot forms low in the flame. The ethylene flame with 23 cc/s of air was unstable, and the soot LII signal-to-noise ratio was too low near the base of the flame to discern soot LII from PAH LIF. The maximum intensities of OH and PAH LIF are nearly

constant for all flames shown, but the maximum soot LII intensity in the ethylene flames increases with airflow, perhaps because buoyant flickering enhances sooting [10] or because of increased high-temperature residence time for soot formation and growth in the longer flames. Soot in the methane flame is not detectable by LII. Both PAH LIF and soot LII intensities are greater for the ethylene than for methane, demonstrating the greater sooting propensity of ethylene.

Summary and Conclusions

Methane and ethylene IDFs with various air flow-rates have been examined using visible images, OH and PAH LIF, and soot LII. Radiation from soot surrounding the IDF was found to mask the reaction zone in visible images. As a result, flame heights determined from visible images were overestimated. The height of the reaction zone as indicated by OH LIF was shown to be a more relevant measure of height. Flame height was found to increase with increasing air flow-rate. A scale analysis considering heat losses and buoyancy yielded predicted flame heights in good agreement with OH LIF flame heights. PAH LIF and soot LII were indistinguishable in methane flames because of very low soot yields. For the ethylene flames, PAH and soot were present on the outside of the IDF in the fuel rich region, and soot was present closer to the reaction zone than PAH. Soot formed close to the base of ethylene flames, and longer ethylene flames exhibited higher soot LII signals. The higher soot signals for the longer flames were attributed to increased soot growth during longer residence times at high temperatures. Ethylene flames had higher PAH LIF and soot LII signals than methane flames, demonstrating the greater propensity for ethylene flames to form soot.

Acknowledgements

This research is funded by NASA under multiple contracts. Dr. Douglas Feikema is the technical contact. Dr. Kurt Sacksteder is the technical monitor. Professor Fernandez-Pello and students Petar Kis, Ryan Niblock and Mary Louie from UC Berkeley provided invaluable assistance.

Sandia is a multiprogram laboratory operated by Sandia Corporation, a Lockheed Martin Company, for the United States Department of Energy's National Nuclear Security Administration under Contract DE-AC04-94AL85000.

References

[1] Blevins, L. G., Fernandez, M. G., Mulholland, G. W., Davis, R. W., Moore, E. F., Steel, E. B., and Scott, J. H. J., *Proceedings of the Sixth International Microgravity Combustion Workshop*, NASA, Cleveland, Ohio, 2001.

[2] Blevins, L. G., Mulholland, G. W., and Davis, R. W., *Proceedings of the Fifth International Microgravity Combustion Workshop, NASA/CP-1999-208917*, NASA, Cleveland, 1999, p.479.

[3] Eckbreth, A. C., *Journal of Applied Physics*, 48:4473, 1977.

[4] Frenklach, M, *Physical Chemistry Chemical Physics*, 4:2028, 2002.

[5] Glassman, I., *Combustion,* Academic Press, San Diego, CA, 1996.

[6] Hall, J. R. Jr., National Fire Protection Association (NFPA), Quincy, MA, 1996.

[7] Spotlight. Klimek, R. B. and Wright, T. W. 2003.

[8] Law, C. K. and Faeth, G. M., *Progress in Energy and Combustion Science,* 20:65, 1994.
[9] Santoro, R. J. and Shaddix C.R., *Laser-Induced Incandescence, Applied Combustion Diagnostics,* edited by Kohse-Höinghaus, K., Jeffries, J. B., Taylor & Frances, New York, 2002, Chap. 9, pp. 252-286.
[10] Smyth, K. C., Shaddix C.R., and Everest D.A., *Combustion and Flame,* 111:185, 1997.

Table 1 IDF Operating Conditions

Fuel	**Q_{fuel}**	**Q_{air}**	**V_{fuel}**	**V_{air}**	**V_{air}/V_{fuel}**	**$Re_{fuel,Dc}$**	**$Re_{air,Dair}$**	**$\Phi_{overall}$**	**HRR_{air}**
	Cc/s	**cc/s**	**cm/s**	**cm/s**					**W**
CH_4	64.0	5.0	10.2	6.4	0.6	123	42	122	17
		8.3		10.6	1.0		70	73	29
		20.0		25.5	2.5		169	30	70
		21.7		27.6	2.7		183	28	76
		26.7		33.9	3.3		226	23	93
		28.3		36.1	3.5		240	22	99
		30.0		38.2	3.8		254	20	105
		33.3		42.4	4.2		282	18	116
		36.7		46.7	4.6		310	17	128
		40.0		50.9	5.0		338	15	140
		43.3		55.2	5.4		366	14	151
		45.0		57.3	5.6		381	14	157
C_2H_4	45.3	16.7	7.2	21.2	2.9	165	141	38.8	64.0
		20.0		25.5	3.5		169	32.3	76.8
		23.3		29.7	4.1		197	27.7	89.6
		27.0		34.4	4.8		228	24.0	103.7
		30.0		38.2	5.3		254	21.6	115.2
		33.3		42.4	5.9		282	19.4	128.0
		36.7		46.7	6.5		310	17.6	140.8

Table 2 Detection Schemes

		295 nm long-pass	**340 nm band-pass**	**450 nm short-pass**	**550 nm long-pass**	**gate delay (ns)**	**gain**
OH LIF	**imaging**	√	C_2H_4	CH_4		0	200
OH LIF	**analysis**	√	√			0	200
PAH LIF	**imaging**	√	C_2H_4	CH_4		0	200
PAH LIF	**analysis**	√	√			0	200
soot LII	**imaging**	√			√	200	250
soot LII	**analysis**	√			√	200	250

Figure 1 Visible Images of Selected Methane IDF

Low Point in Flicker Cycle

20 cc/s 27 cc/s 33 cc/s 37 cc/s 40 cc/s 43 cc/s

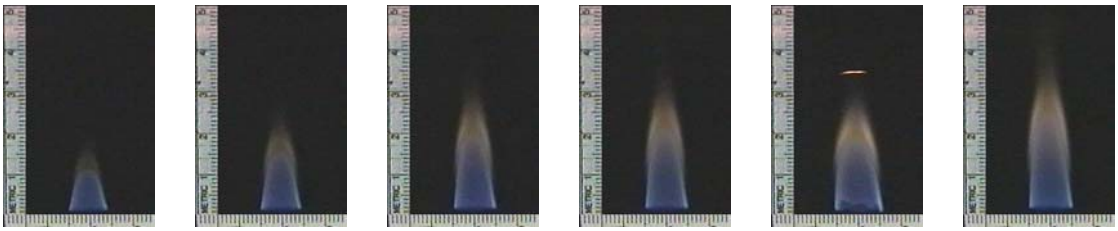

High Point in Flicker Cycle

20 cc/s 27cc/s 33 cc/s 37 cc/s 40 cc/s 43 cc/s

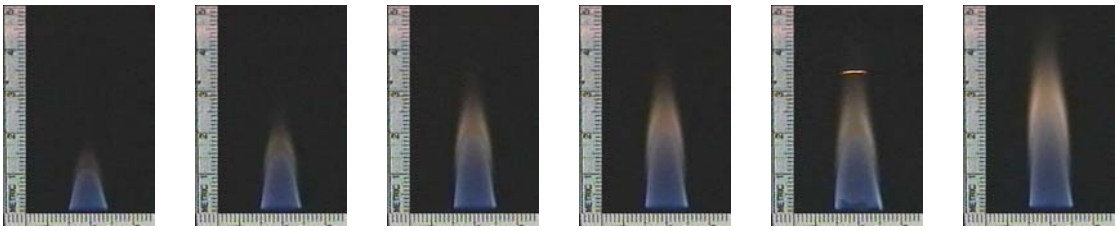

Note: The horizontal line in 40 cc/s image is a glowing thermocouple wire.

Figure 2 Visible Images of Selected Ethylene IDF

Low Point in Flickering Cycle

17 cc/s 20 cc/s 23 cc/s 27 cc/s 33 cc/s 37 cc/s

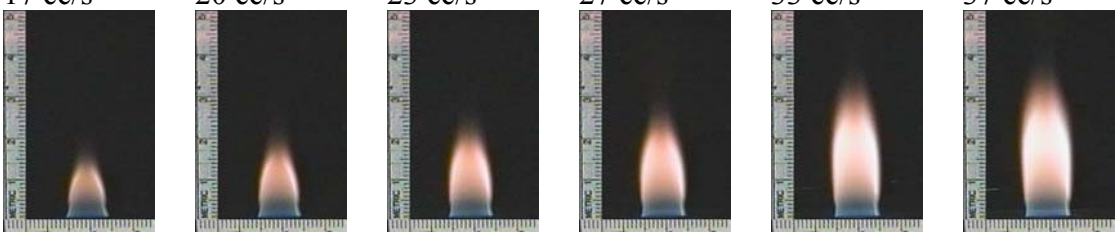

High Point in Flickering Cycle

17 cc/s 20 cc/s 23 cc/s 27 cc/s 33 cc/s 37 cc/s

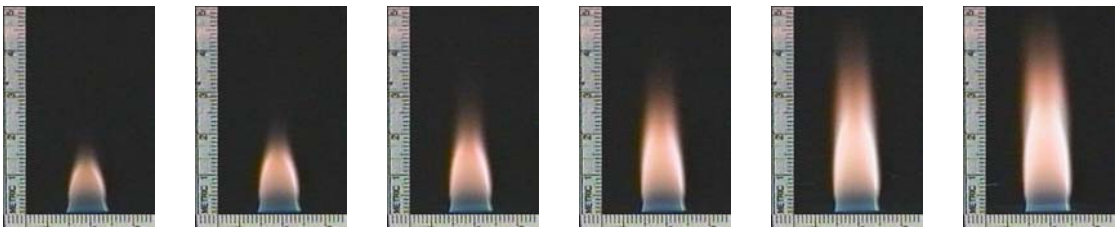

Figure 3 OH and PAH LIF of Methane IDF with 450-nm Filter

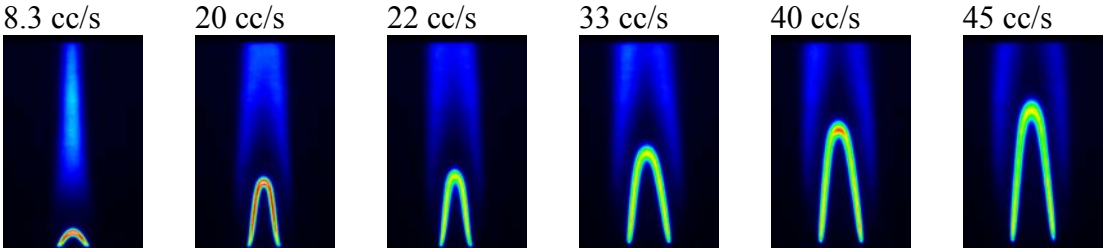

Figure 4 OH and PAH LIF of Ethylene IDF with 340-nm Filter

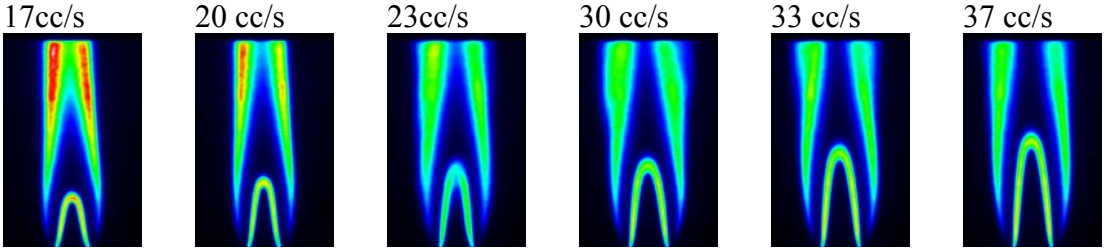

Figure 5 Flame Heights of Methane and Ethylene IDF

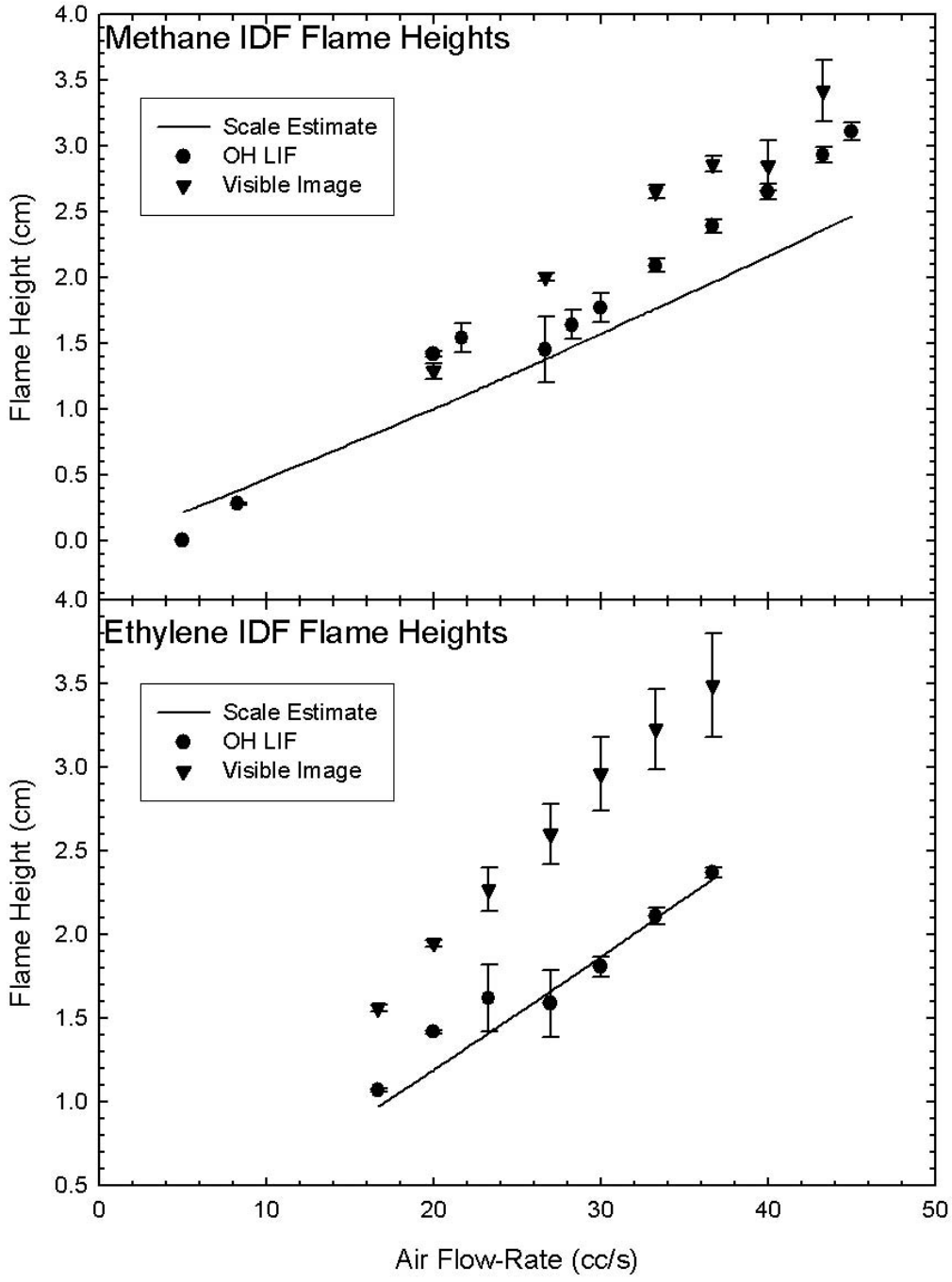

Figure 6 PAH LIF and Soot LII of Methane IDF with 550-nm Filter

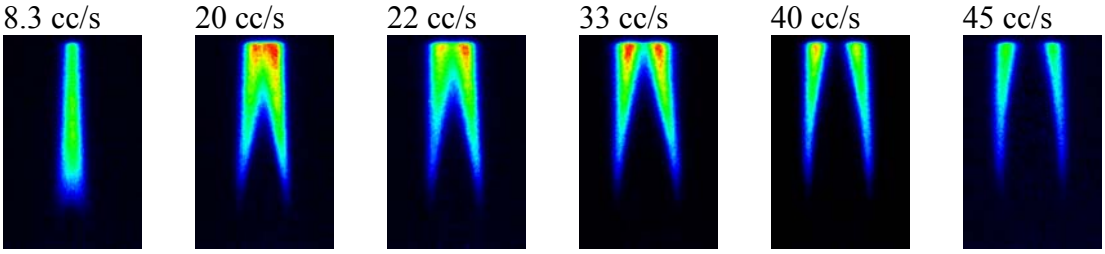

Figure 7 PAH LIF and Soot LII of Ethylene IDF with 550-nm Filter

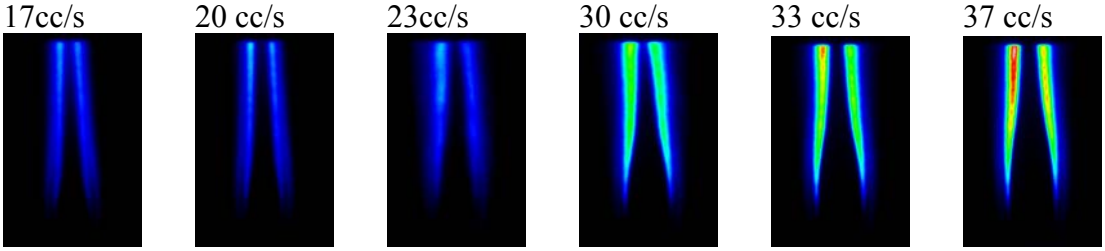

Figure 8 Position of PAH LIF, OH LIF and Soot LII Maximum Intensity, Maximum PAH LIF, OH LIF and Soot LII Intensity versus Axial Position, Ethylene IDF

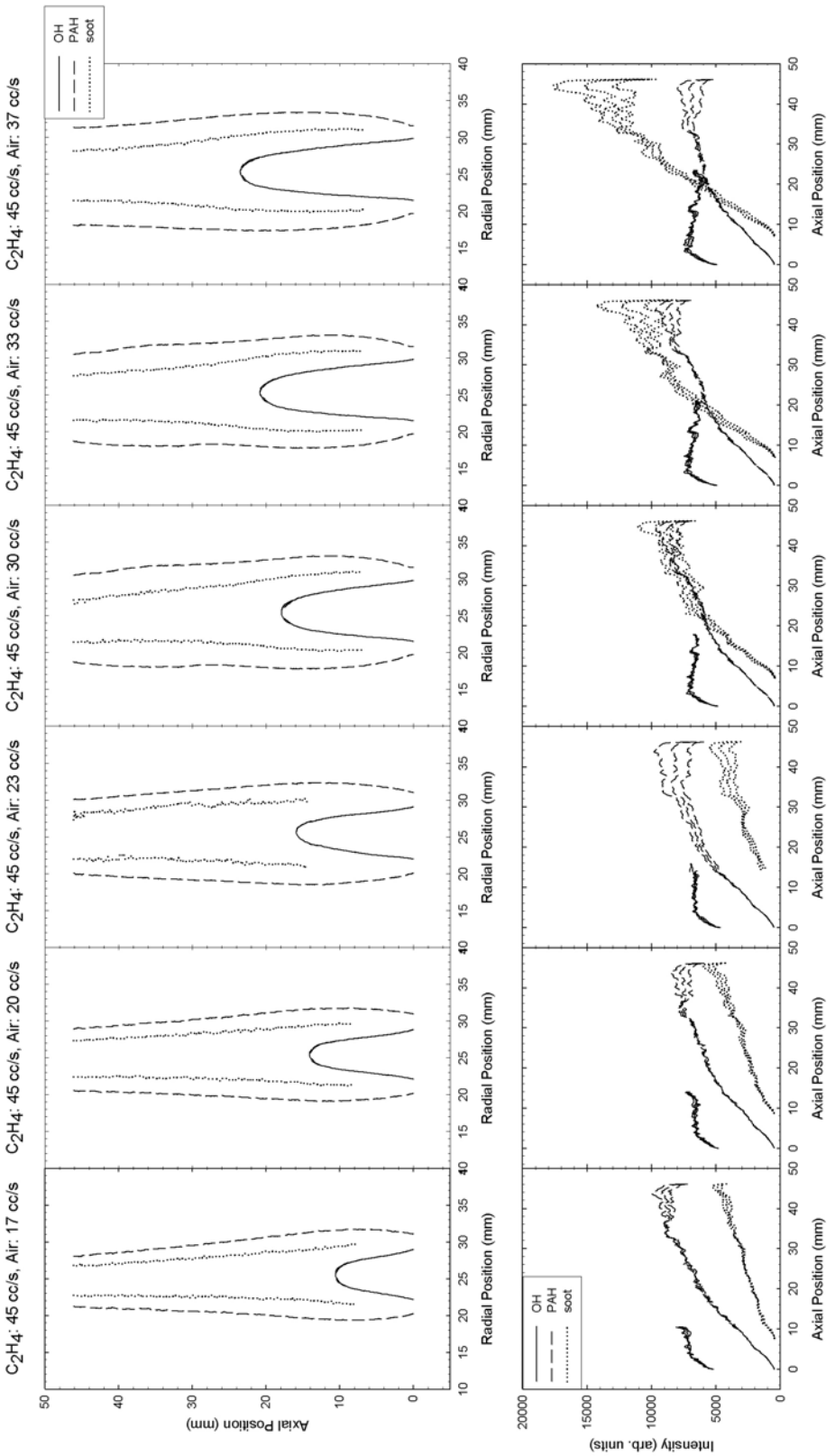

Figure 9 Position of PAH LIF, OH LIF and Soot LII Maximum Intensity, Maximum PAH LIF, OH LIF and Soot LII Intensity versus Axial Position, Methane IDF